Thermal-stimulated spin disordering accelerates water electrolysis

Fakang Xie,[‡a] Yu Du,[‡a] Mengfei Lu,[b] Shicheng Yan,[*a,b] and , Zhigang Zou[a,b]

[a.] Collaborative Innovation Center of Advanced Microstructures, National Laboratory of Solid State Microstructures, College of Engineering and Applied Sciences, Nanjing University, No. 22 Hankou Road, Nanjing, Jiangsu 210093, P. R. China. E-mail: yscfei@nju.edu.cn
[b.] Jiangsu Key Laboratory for Nano Technology, Nanjing University, No. 22 Hankou Road, Nanjing, Jiangsu 210093, P. R. China
[‡] These authors contributed equally to this work.

Table of Contents

Figures

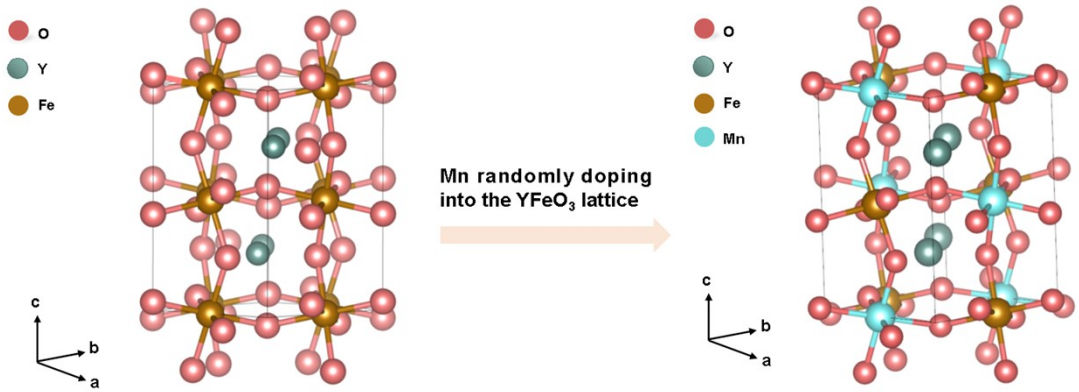

Fig. S1 The crystal structures of $YFeO_3$ and $YFe_{1-x}Mn_xO_3$.

In $YFeO_3$ unit cell, crystallizing in an orthorhombically distorted perovskite structure with the space group Pnma[1], eight FeO_6 octahedra units locate at the eight apexes of unit cell and they share the oxygen atom at their common apex of two adjacent octahedra[2]. The Y toms with large radius are located in eight octahedral voids. Mn doping is achieved by randomly replacing Fe in the lattice of $YFeO_3$ to form a solid solution.

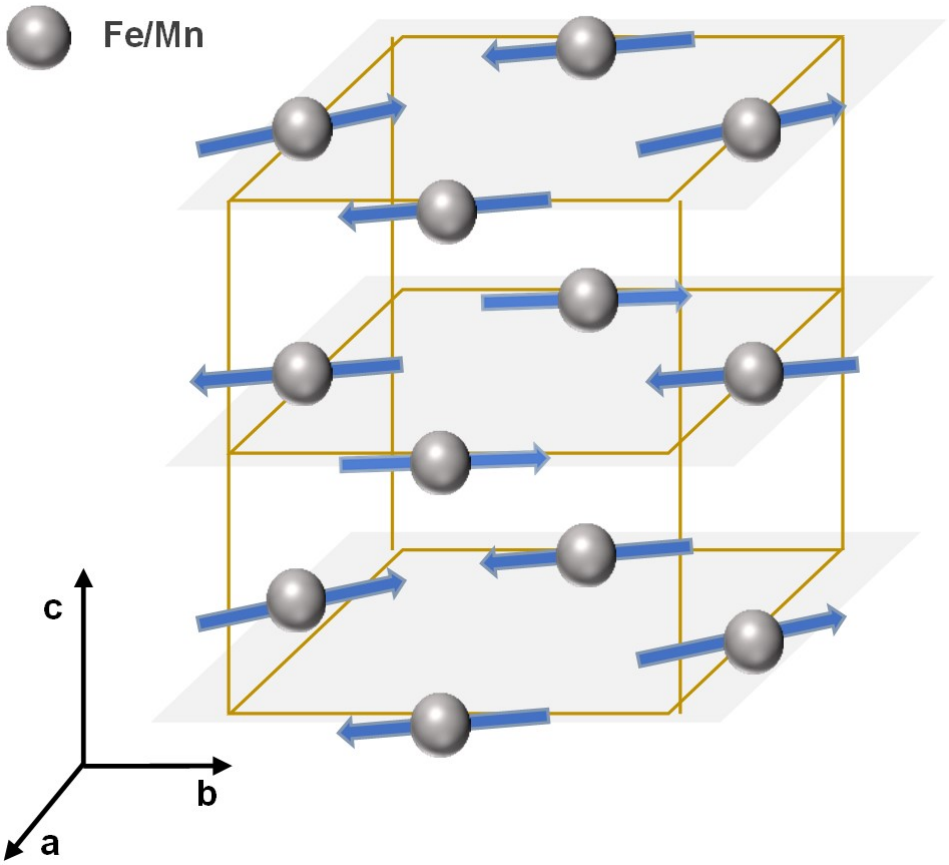

Fig. S2 The spin structures of Fe^{3+}/Mn^{3+} spins at AFM state.

The magnetic structures of antiferromagnetism can generally be divided into the following types[3]:

- G-AFM (Geometric Antiferromagnetism): Refers to an antiferromagnetic structure where the atomic magnetic moments are arranged in a geometric pattern in space.
- C-AFM (Cubic Antiferromagnetism): Refers to an antiferromagnetic arrangement in a cubic crystal system, where the atomic magnetic moments are aligned in opposite directions on adjacent atoms.
- A-AFM (Body-Centered Antiferromagnetism): Refers to an antiferromagnetic arrangement in a body-centered cubic crystal system, where the atomic magnetic moments are aligned in opposite directions between the body center and the corners.
- E-AFM (Face-Centered Antiferromagnetism): Refers to an antiferromagnetic arrangement in a face-centered cubic crystal system, where the atomic magnetic moments are aligned in opposite directions between the face centers and the adjacent corners.
- S-AFM (Spiral Antiferromagnetism): Refers to a structure where atomic magnetic moments are arranged in a spiral pattern, forming a spin spiral structure.
- T-AFM (Triangular Antiferromagnetism): Refers to an antiferromagnetic arrangement in a triangular crystal system, where the atomic magnetic moments are aligned in opposite directions on adjacent atoms.

According to temperature-dependent magnetization data and neutron diffraction data, the magnetic ground state of $YFe_{1-x}Mn_xO_3$ belongs to G-AFM (Figure S2)[1].

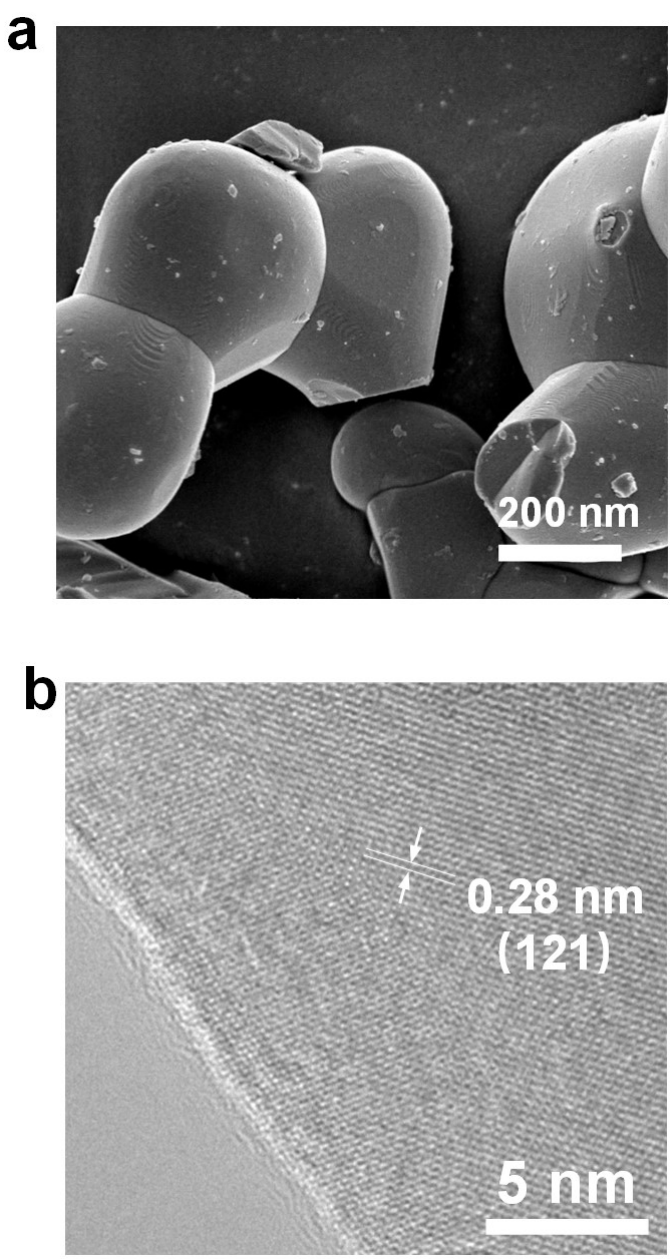

Fig. S3 (a) SEM image and (b) HRTEM image of $YFe_{0.6}Mn_{0.4}O_3$.

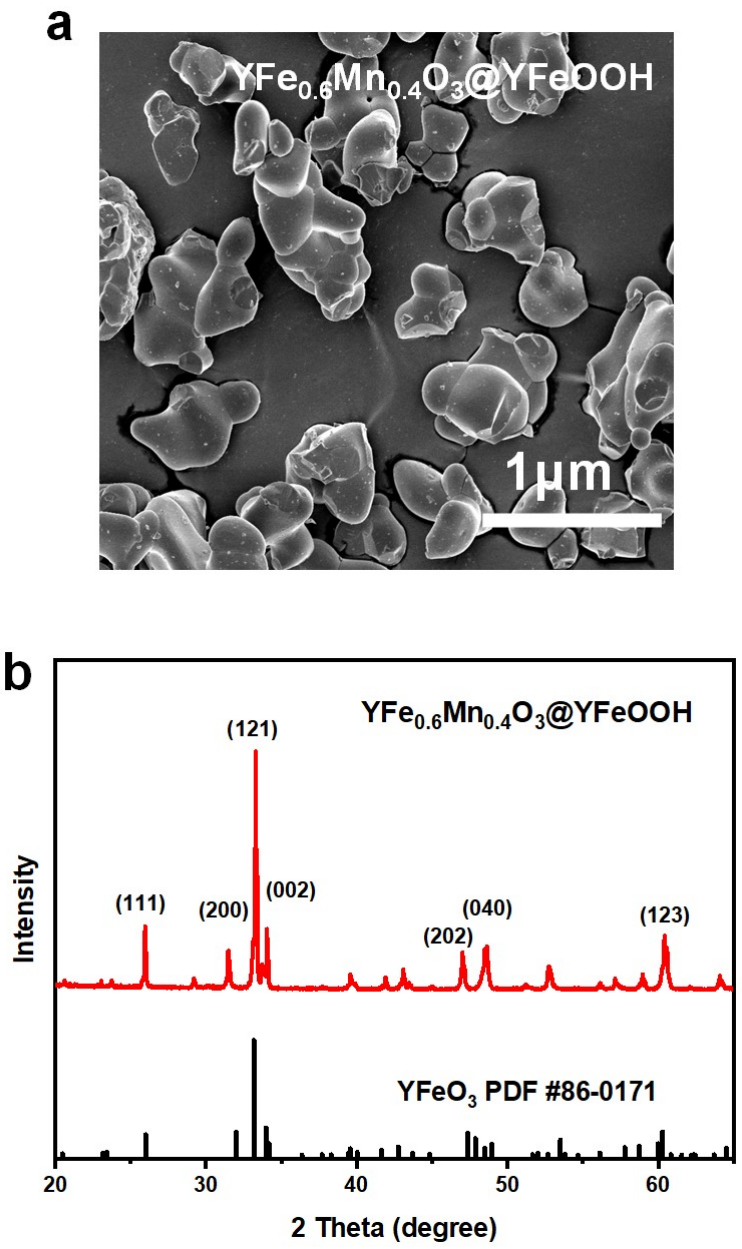

Fig. S4 (a) SEM image image of $YFe_{0.6}Mn_{0.4}O_3$@YFeOOH. (b) XRD pattern of $YFe_{0.6}Mn_{0.4}O_3$@YFeOOH.

After the electrochemical activation of $YFe_{0.6}Mn_{0.4}O_3$ at an OER potential of 1.6 V for 20 minutes in a 1 M KOH electrolyte under 90°C , $YFe_{0.6}Mn_{0.4}O_3$@YFeOOH maintains a similar morphology and structure to the original $YFe_{0.6}Mn_{0.4}O_3$. XRD (X-ray diffraction) analysis still shows the same characteristic peaks

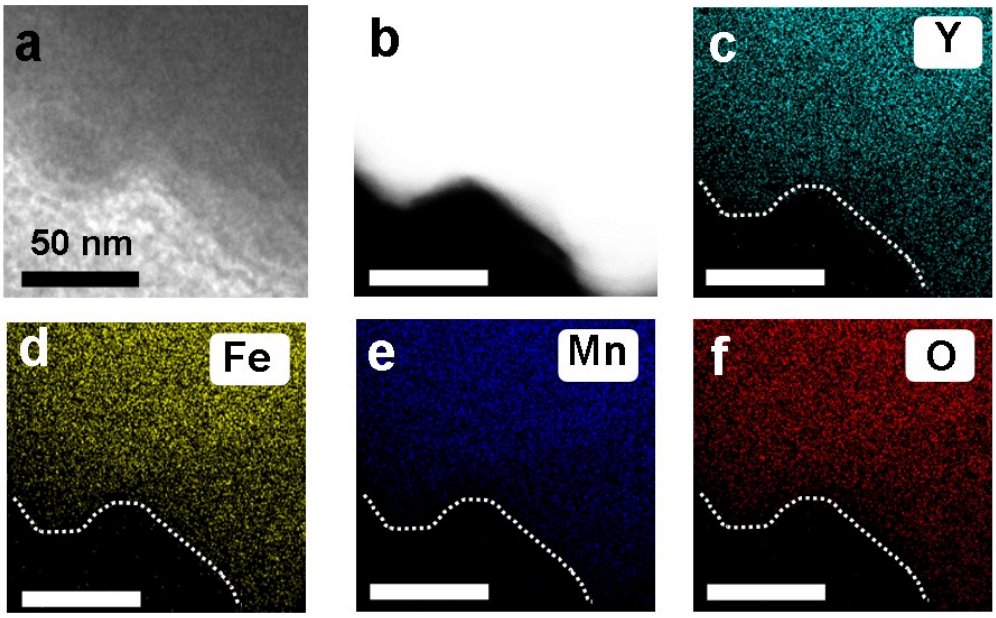

Fig. S5 HAADF-STEM image of the $YFe_{0.6}Mn_{0.4}O_3$@YFeOOH particle (a, b), and the Y (c), Fe (d), Mn (e), and O (f) distributions in $YFe_{0.6}Mn_{0.4}O_3$@YFeOOH particle.

The compositions of the $YFe_{0.6}Mn_{0.4}O_3$ after electrochemical activation were further determined by the high angle annular dark field scanning transmission electron microscopy (HAADF-STEM) image and elemental mapping. Obviously, the amorphous layer comprises of uniformly dispersed Y, Fe, and O elements, but Mn element nearly misses in this layer.

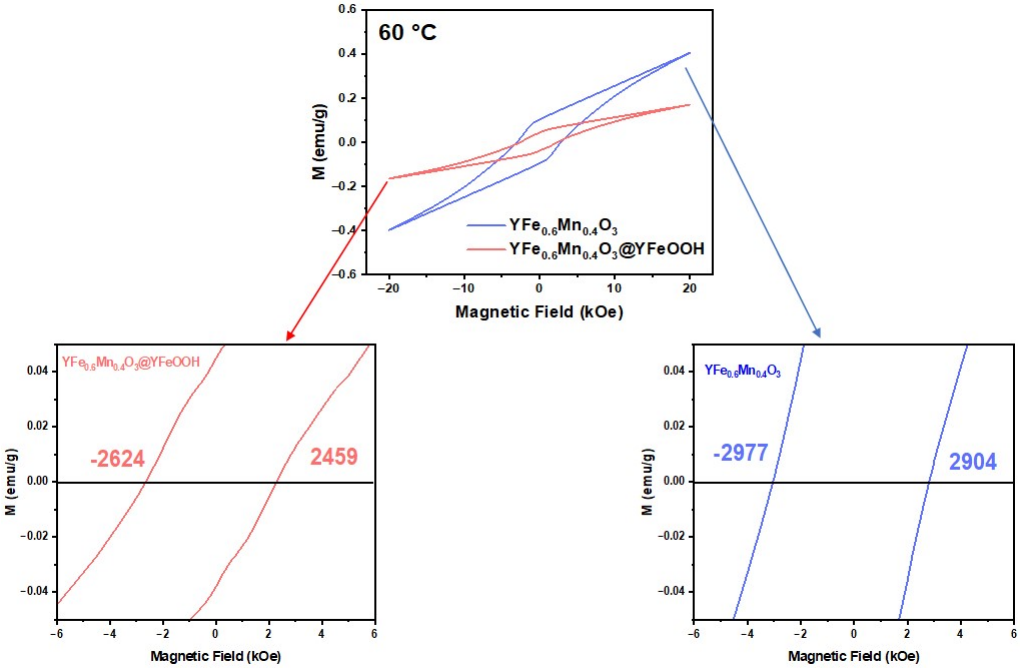

Fig. S6 Magnetic hysteresis loops for $YFe_{0.6}Mn_{0.4}O_3$ and $YFe_{0.6}Mn_{0.4}O_3$@YFeOOH at 60 °C.

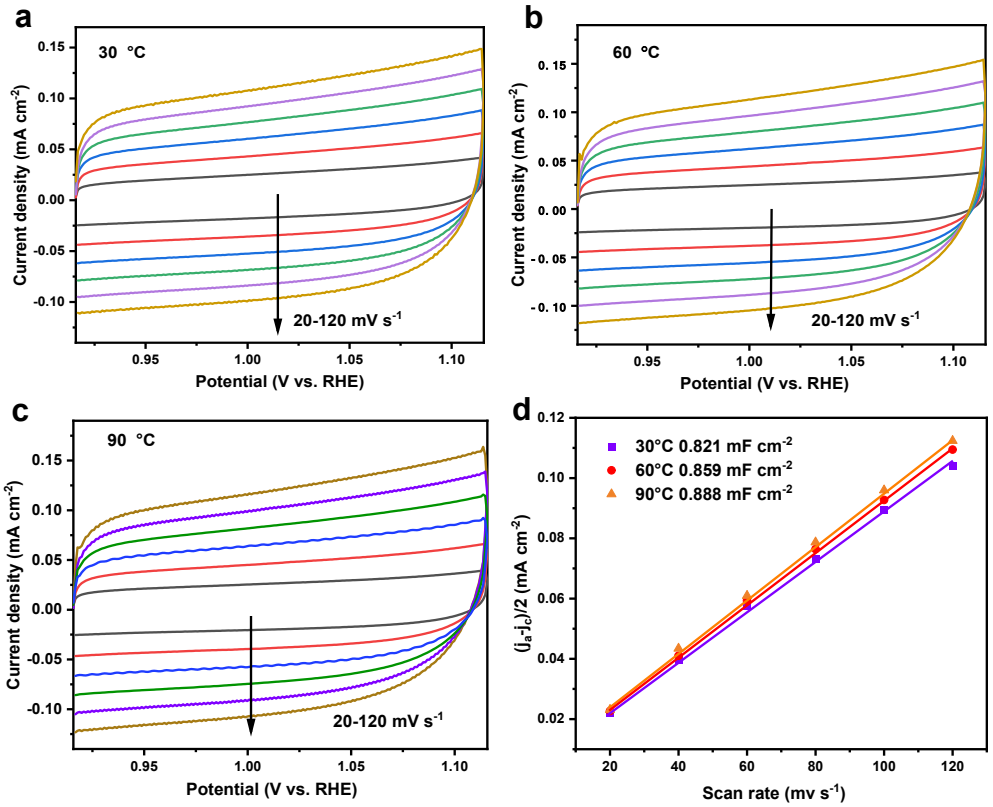

Fig. S7 (a-c) CV curves of $YFe_{0.6}Mn_{0.4}O_3$@YFeOOH with different scan rates in non-faradic region under (a) 30 °C, (b) 60 °C, (c) 90 °C. (d) The non-faraday current density at 1.0 V as a function of scan rates of $YFe_{0.6}Mn_{0.4}O_3$@YFeOOH. The slope of fitting line is the double-layer capacitance.

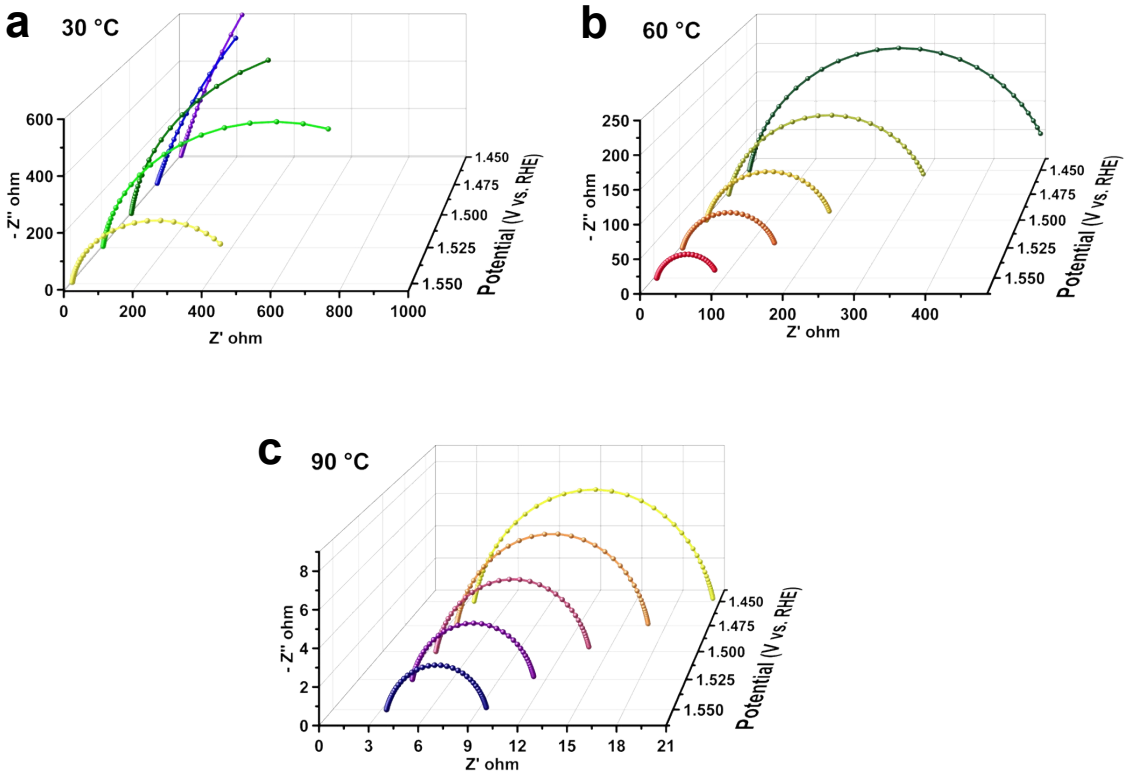

Fig. S8 Temperature-dependent EIS spectra for $YFe_{0.6}Mn_{0.4}O_3$@YFeOOH at. (a) 30 °C, (b) 60 °C, (c) 90 °C in the potential ranges of 1.450 ~ 1.550 V vs RHE.

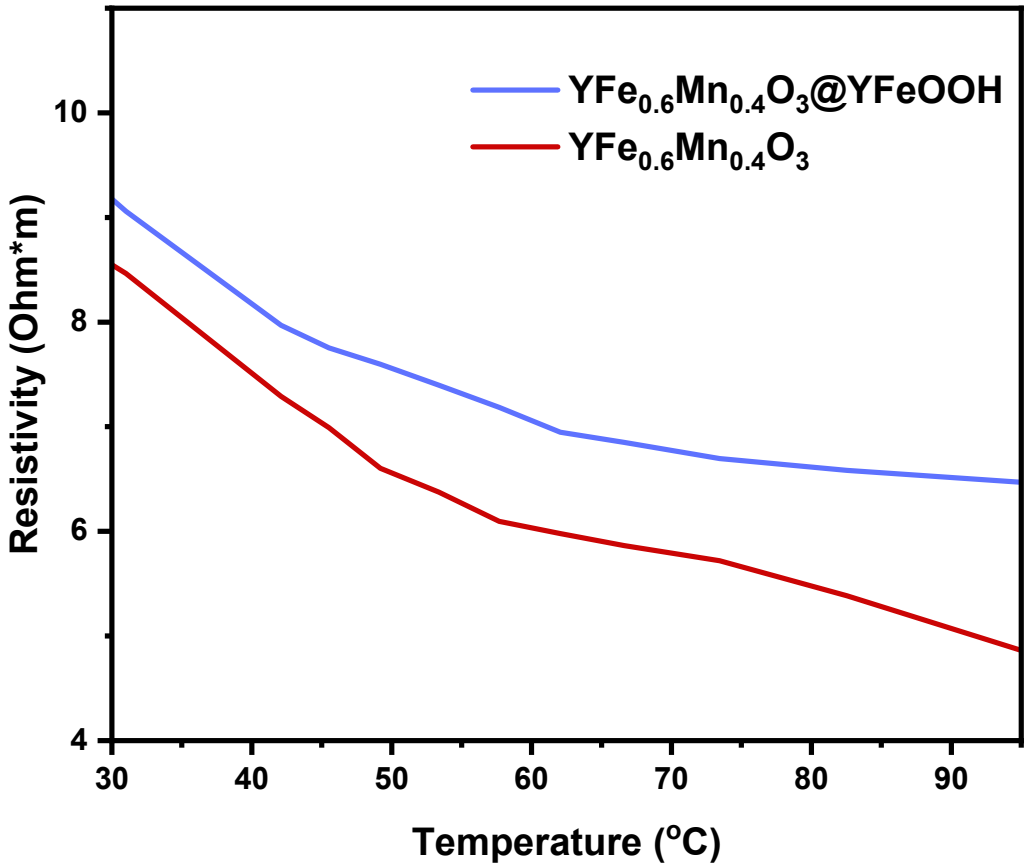

Fig. S9 Temperature-dependent resistivity of $YFe_{0.6}Mn_{0.4}O_3$ and $YFe_{0.6}Mn_{0.4}O_3$@YFeOOH.

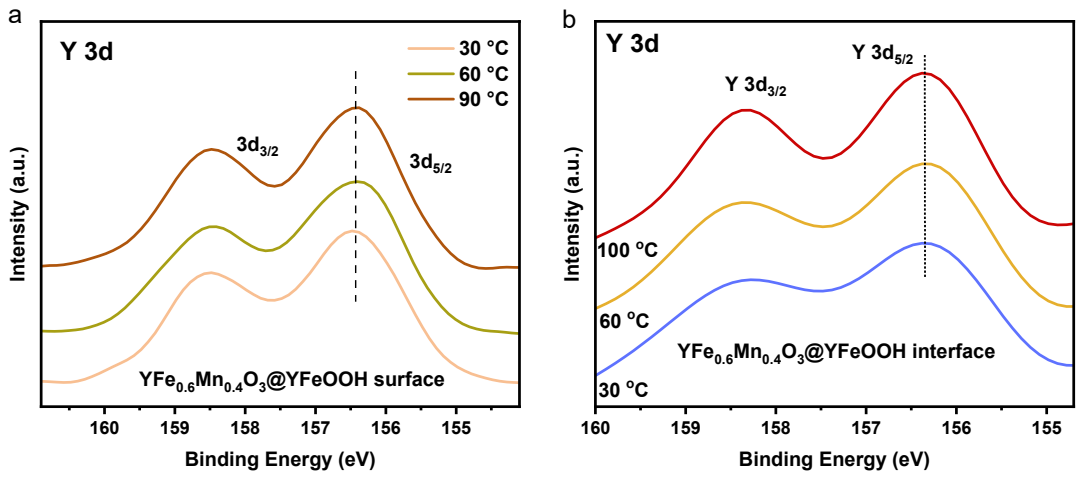

Fig. S10 (a) Y 3d XPS spectra for $YFe_{0.6}Mn_{0.4}O_3$@YFeOOH at different temperatures. (b) Y 3d XPS spectra for $YFe_{0.6}Mn_{0.4}O_3$@YFeOOH at different temperatures after 6 nm etching.

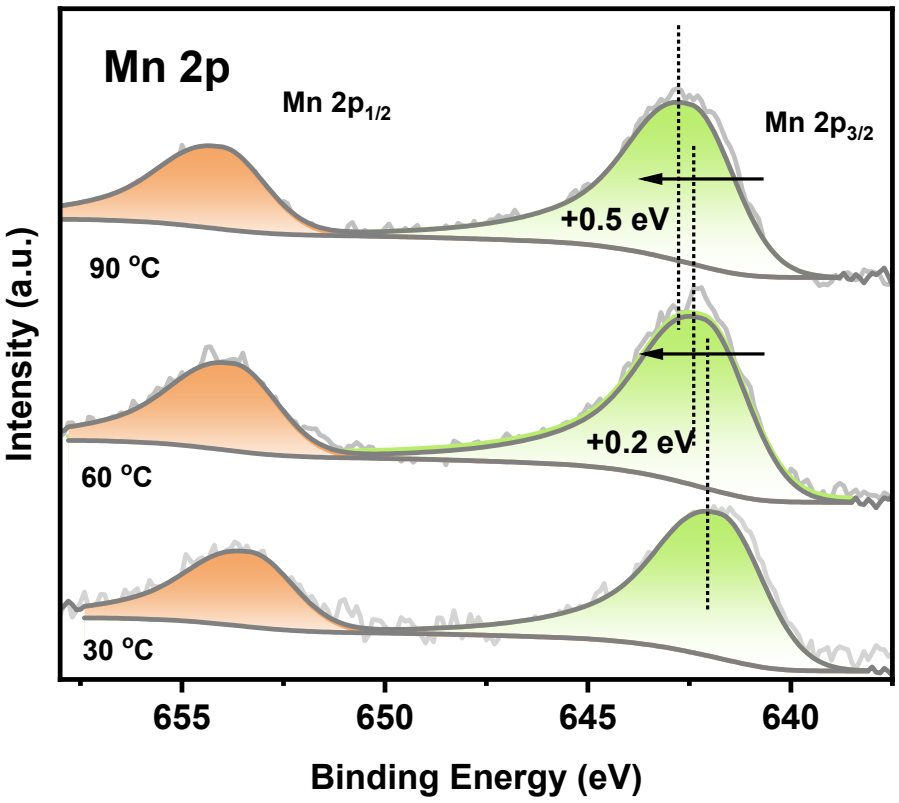

Fig. S11 Mn 2p XPS spectra for $YFe_{0.6}Mn_{0.4}O_3$@YFeOOH at different temperatures after 6 nm etching.

Fe 2p, Y 3d, and Mn 2p XPS (X-ray photoelectron spectroscopy) spectra were conducted on $YFe_{0.6}Mn_{0.4}O_3$@YFeOOH at various temperatures following a 6 nm etching process. It was observed that at the interface between $YFe_{0.6}Mn_{0.4}O_3$ and YFeOOH, the binding energy shifts of both Fe and Mn exhibit temperature dependence, while the binding energy of Y remains largely unaffected by temperature changes. Compared to the in situ Fe2p XPS data at the surface of $YFe_{0.6}Mn_{0.4}O_3$@YFeOOH, the binding energy shift of Fe2p at the interface after 6 nm etching is more significantly influenced by temperature. This indicates that the strong interfacial interactions, possibly induced by thermal-simulated magnetic disordering, cause the Fe2p binding energy to shift towards higher values.

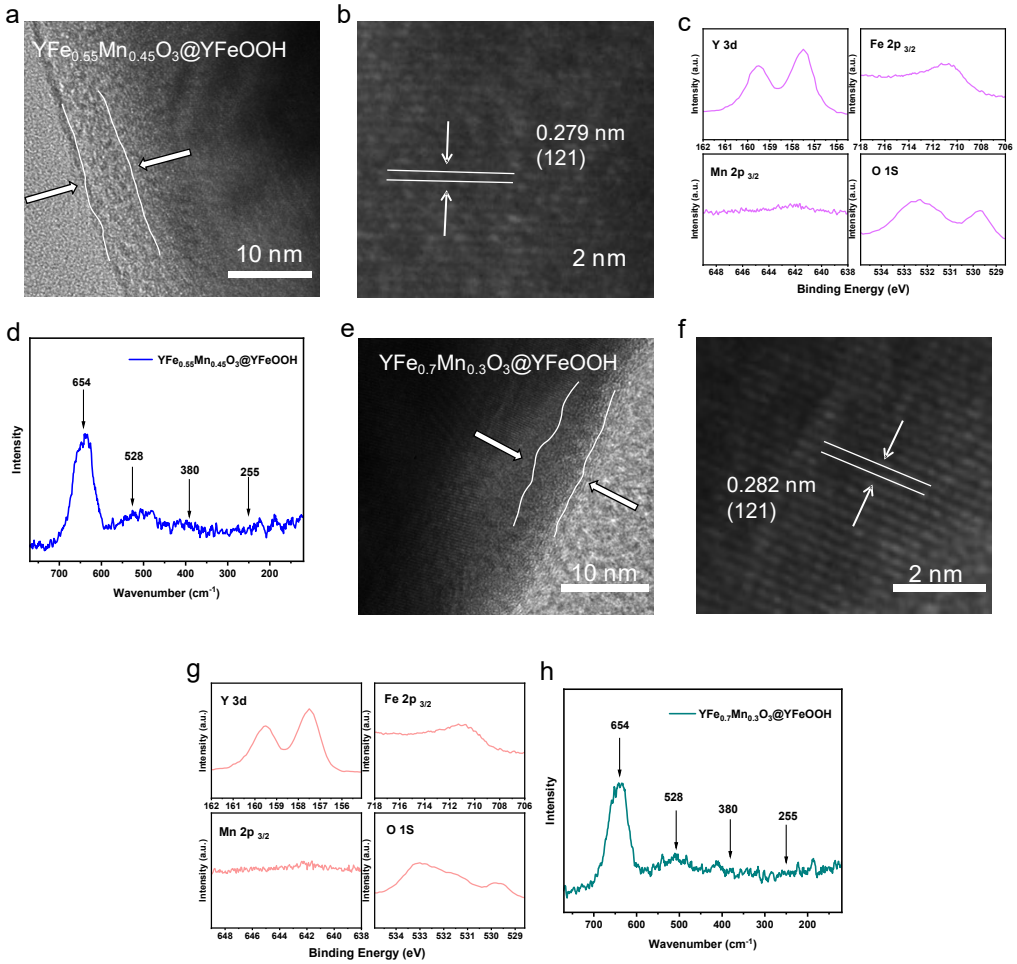

Fig. S12 (a) HRTEM image, (b) High-resolution lattice image, (c) Y 3d, Fe 2p, Mn 2p, O 1s XPS spectra, (d) Raman spectrum for $YFe_{0.55}Mn_{0.45}O_3$ after OER. (e) HRTEM image, (f) High-resolution lattice image, (g) Y 3d, Fe 2p, Mn 2p, O 1s XPS spectra, (h) Raman spectrum $YFe_{0.7}Mn_{0.3}O_3$ after OER.

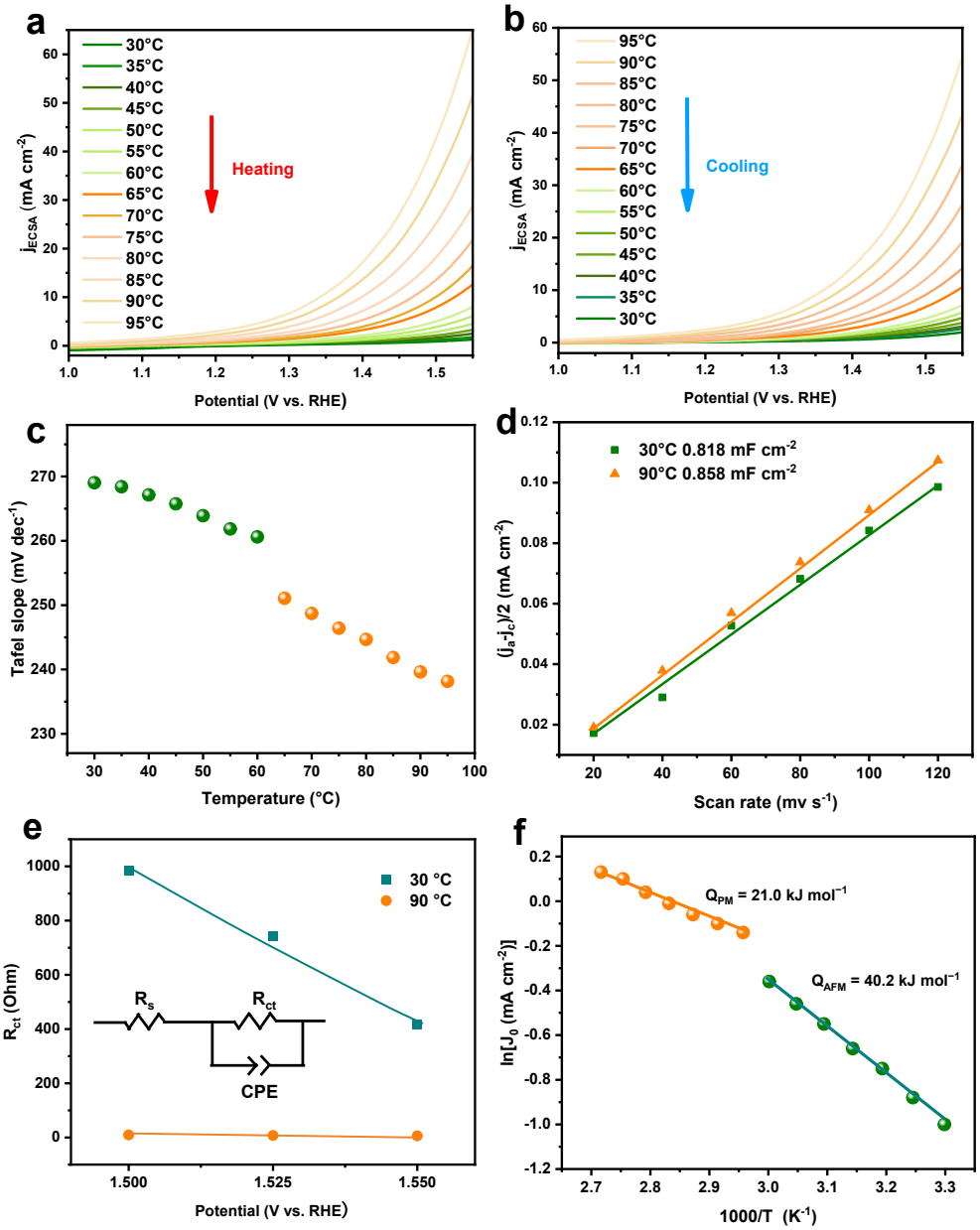

Fig. S13 Heat-electricity coupling for accelerating the OER kinetics of $YFe_{0.55}Mn_{0.45}O_3$@YFeOOH from 30 to 95 ℃. (a) LSV curves normalized with ECSA for $YFe_{0.55}Mn_{0.45}O_3$@YFeOOH with 95% iR correction in 1.0 M KOH during heating. (b) LSV curves normalized with ECSA for $YFe_{0.55}Mn_{0.45}O_3$@YFeOOH with 95% iR correction in 1.0 M KOH during cooling. (c) Temperature-dependent Tafel slopes. (d) The non-faraday current density at 1.10 V as a function of scan rates of $YFe_{0.55}Mn_{0.45}O_3$@YFeOOH. The slope of fitting line is the double-layer capacitance (e) Temperature-dependent R_{ct} fitted from EIS data in the potential regions of water oxidation. Inset shows the Randle's equivalent circuit. (f) Calculated lnj_0-T^{-1} plot with nonlinear Arrhenius relationship for OER on $YFe_{0.55}Mn_{0.45}O_3$@YFeOOH.

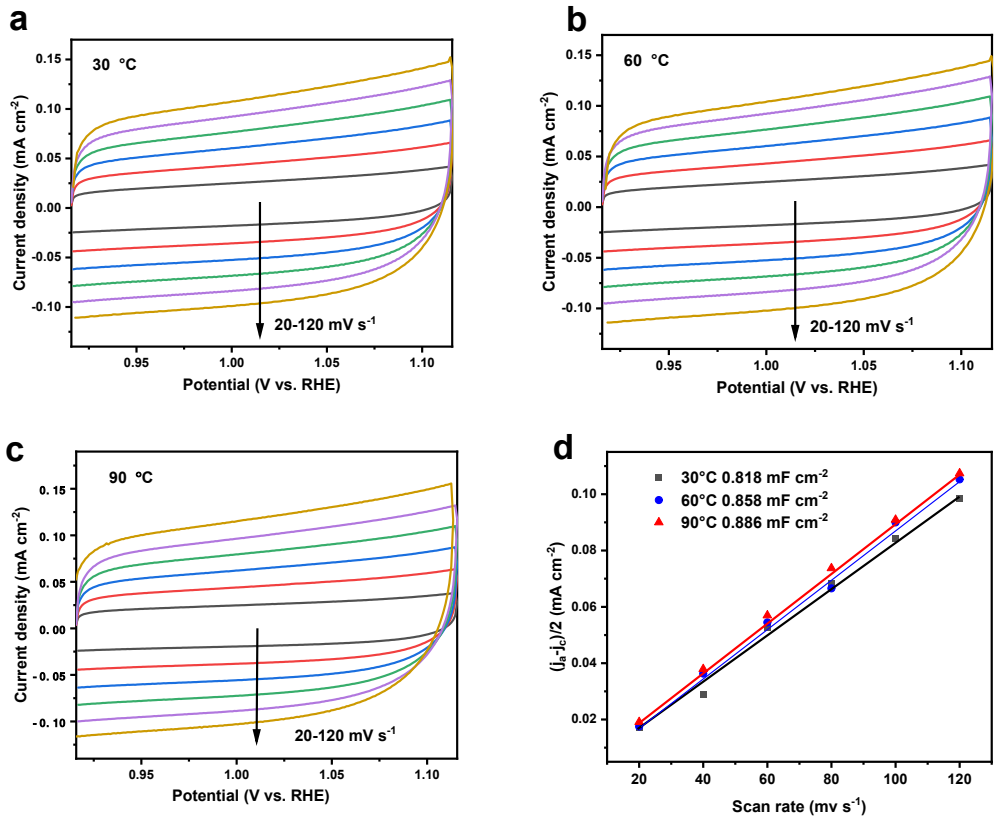

Fig. S14 (a-c) CV curves of $YFe_{0.55}Mn_{0.45}O_3$@YFeOOH with different scan rates in non-faradic region under (a) 30 ℃, (b) 60 ℃, (c) 90 ℃. (d) The non-faraday current density at 1.0 V as a function of scan rates of $YFe_{0.55}Mn_{0.45}O_3$@YFeOOH. The slope of fitting line is the double-layer capacitance.

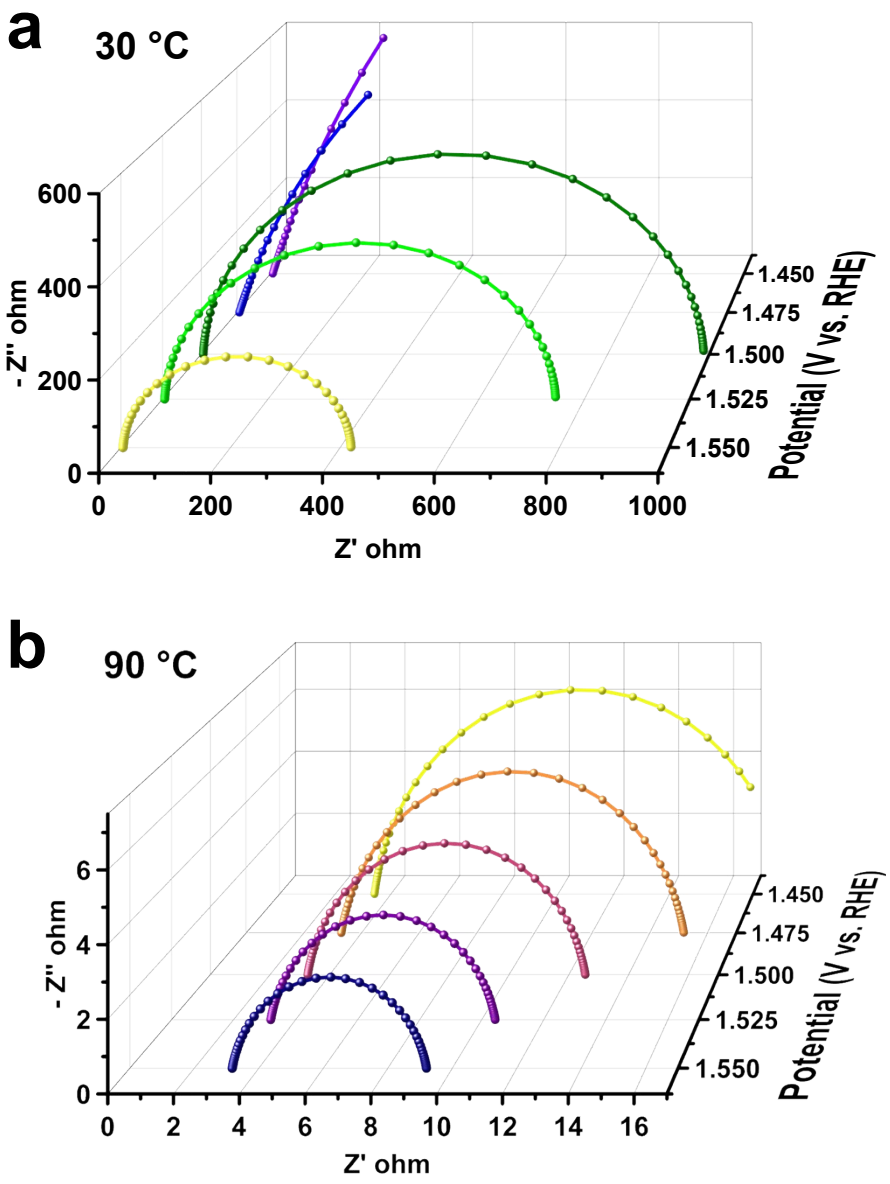

Fig. S15 Temperature-dependent Nyquist plots for $YFe_{0.55}Mn_{0.45}O_3$@YFeOOH at (a) 30 °C, and (b) 90 °C in the potential range of 1.450~1.550 V vs RHE.

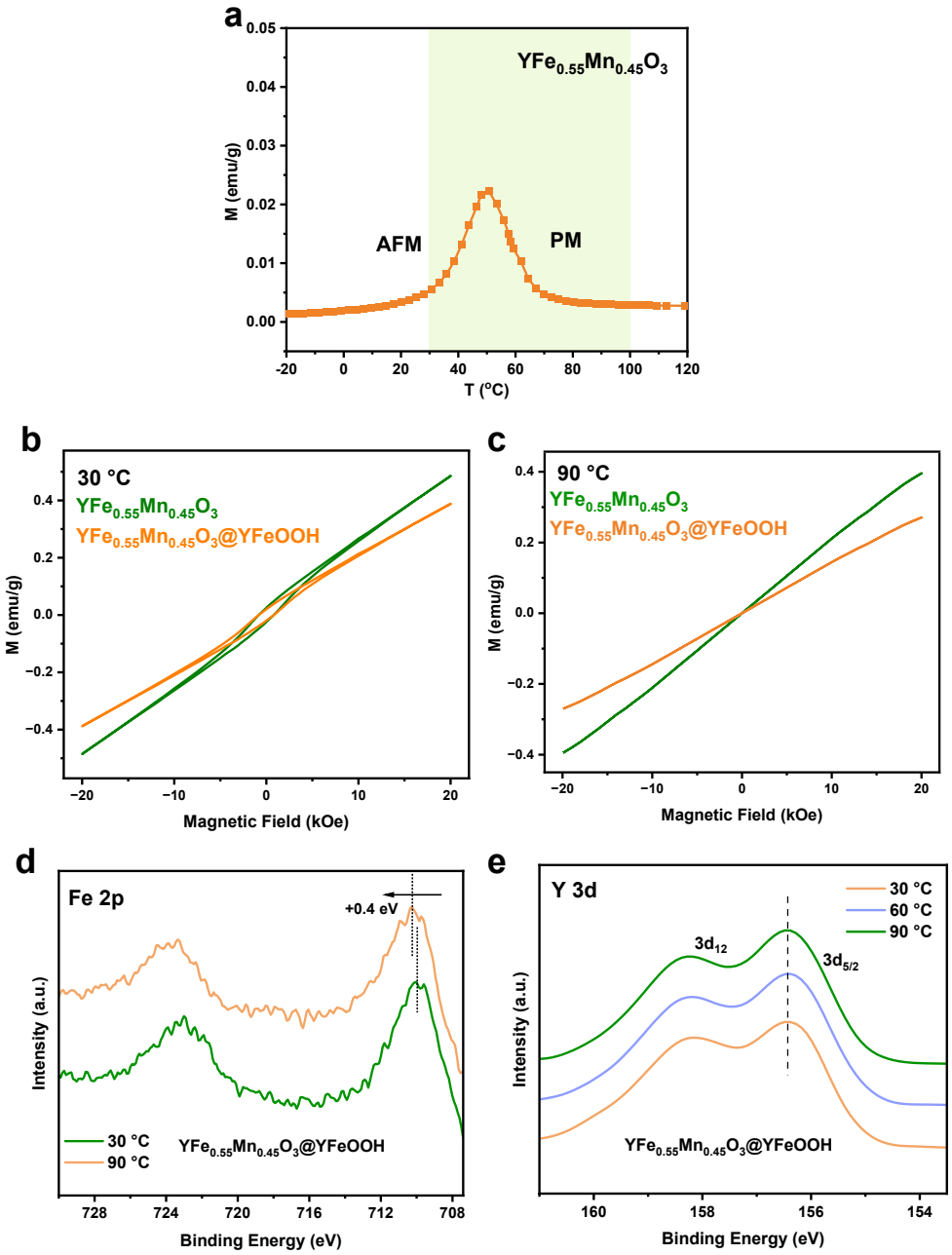

Fig. S16 The influence of temperature on the magnetic properties of $YFe_{0.55}Mn_{0.45}O_3$ and elemental valence states of $YFe_{0.55}Mn_{0.45}O_3$@YFeOOH. (a) Field cooled magnetization curves for $YFe_{0.55}Mn_{0.45}O_3$ at an applied field of 100 Oe. (b, c) Magnetic hysteresis loops for $YFe_{0.55}Mn_{0.45}O_3$ and $YFe_{0.55}Mn_{0.45}O_3$@YFeOOH at 30 °C and 90 °C. (d) Fe 2p and Y 3d XPS spectra for $YFe_{0.55}Mn_{0.45}O_3$@YFeOOH at different temperatures.

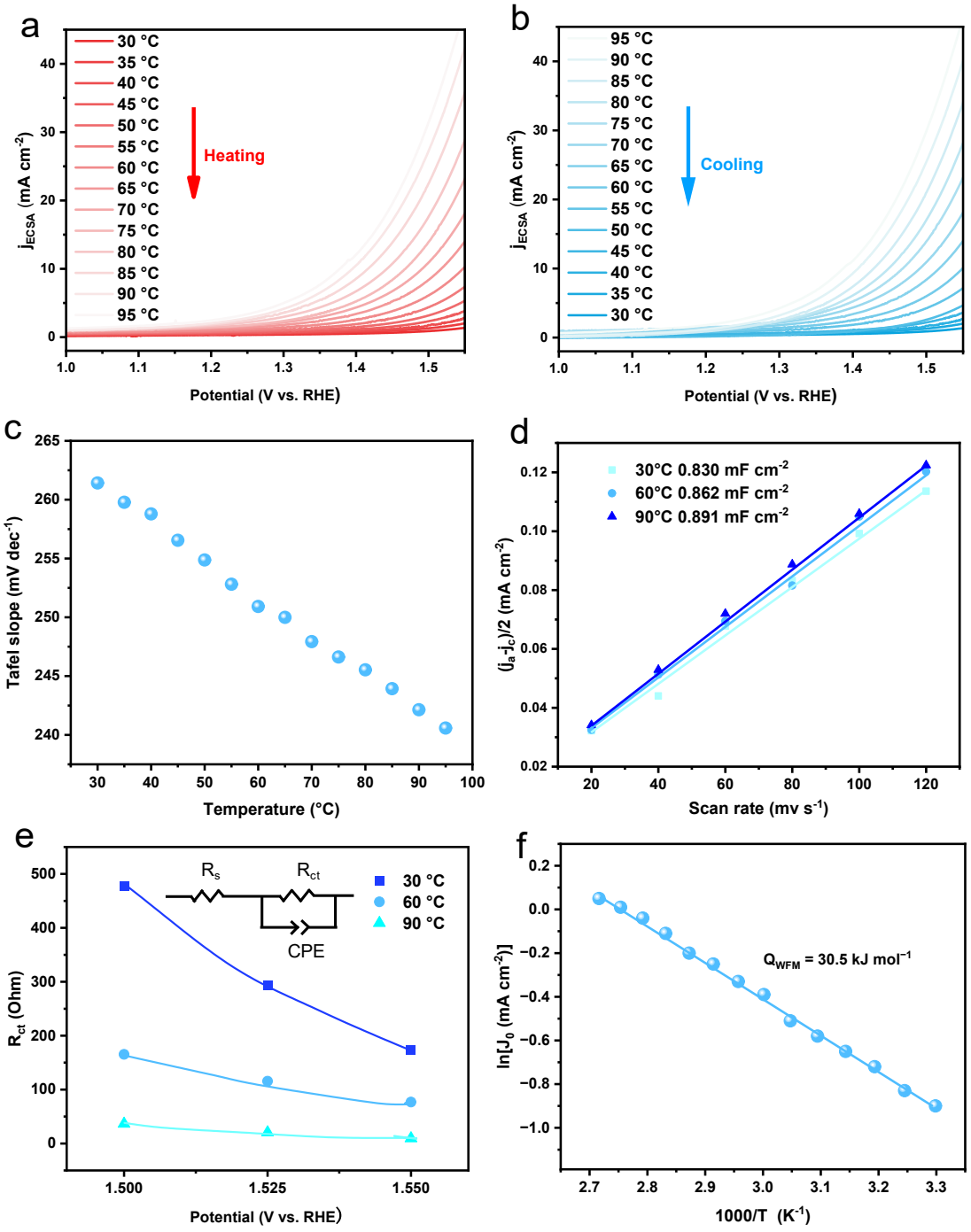

Fig. S17 Heat-electricity coupling for accelerating the OER kinetics of $YFe_{0.7}Mn_{0.3}O_3$@YFeOOH from 30 to 95 °C. (a) LSV curves normalized with ECSA for $YFe_{0.7}Mn_{0.3}O_3$@YFeOOH with 95% iR correction in 1.0 M KOH during heating. (b) LSV curves normalized with ECSA for $YFe_{0.7}Mn_{0.3}O_3$@YFeOOH with 95% iR correction in 1.0 M KOH during cooling. (c) Temperature-dependent Tafel slopes. (d) The non-faraday current density at 1.10 V as a function of scan rates of $YFe_{0.7}Mn_{0.3}O_3$@YFeOOH. The slope of fitting line is the double-layer capacitance (e) Temperature-dependent R_{ct} fitted from EIS data in the potential regions of water oxidation. Inset shows the Randle's equivalent circuit. (f) Calculated lnj_o-T^{-1} plot with linear Arrhenius relationship for OER on $YFe_{0.7}Mn_{0.3}O_3$@YFeOOH.

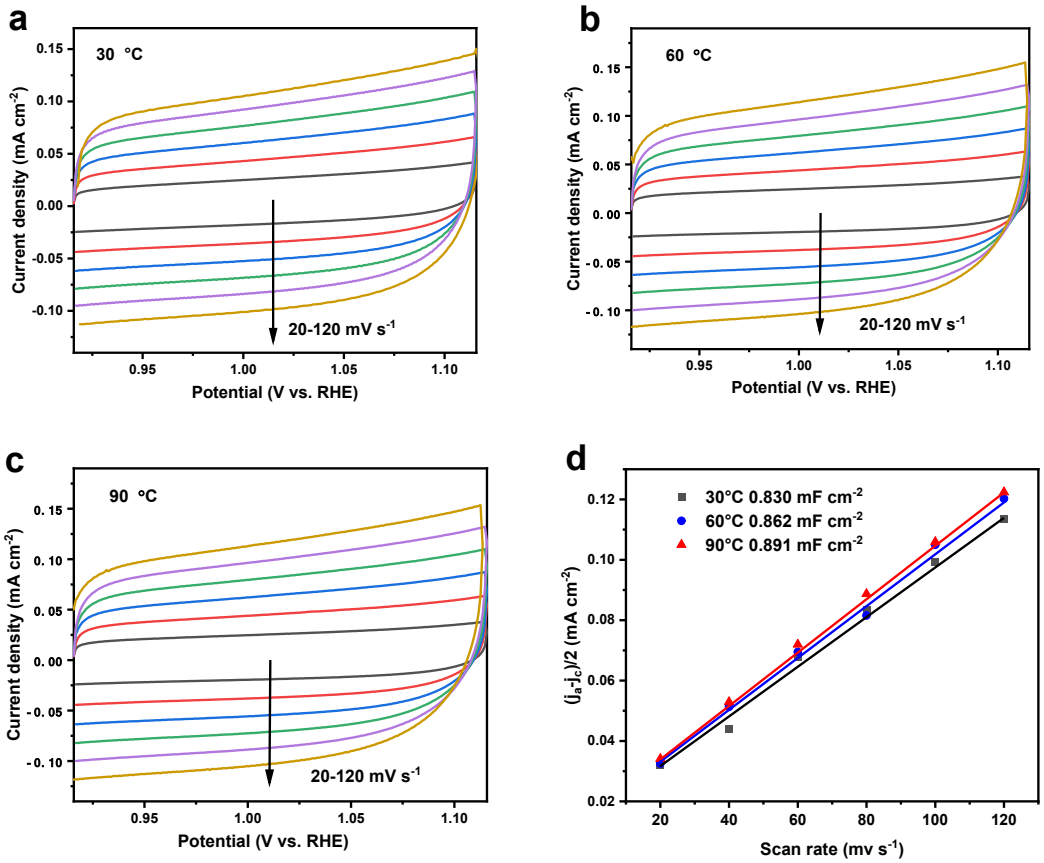

Fig. S18 (a-c) CV curves of $YFe_{0.7}Mn_{0.3}O_3$@YFeOOH with different scan rates in non-faradic region under (a) 30 ℃, (b) 60 ℃, (c) 90 ℃. (d) The non-faraday current density at 1.0 V as a function of scan rates of $YFe_{0.7}Mn_{0.3}O_3$@YFeOOH. The slope of fitting line is the double-layer capacitance.

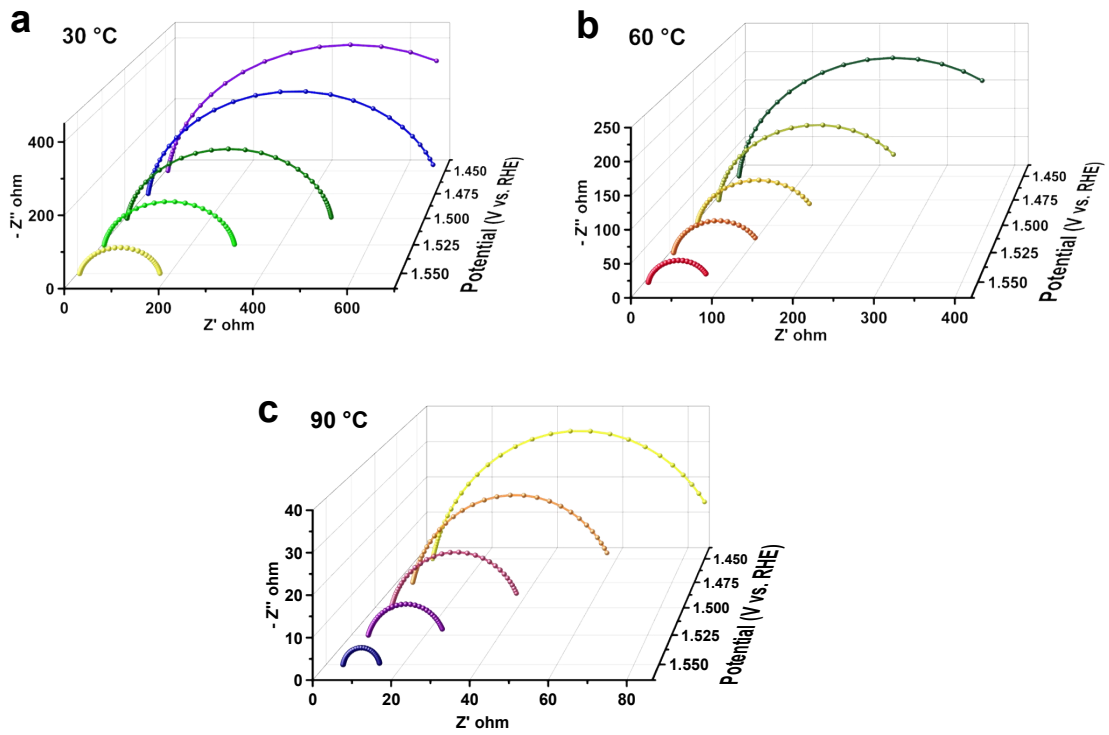

Fig. S19 Temperature-dependent Nyquist plots for $YFe_{0.7}Mn_{0.3}O_3$@YFeOOH at (a) 30 °C, (b) 60 °C, and (c) 90 °C in the potential ranges of 1.450~1.550 V vs RHE.

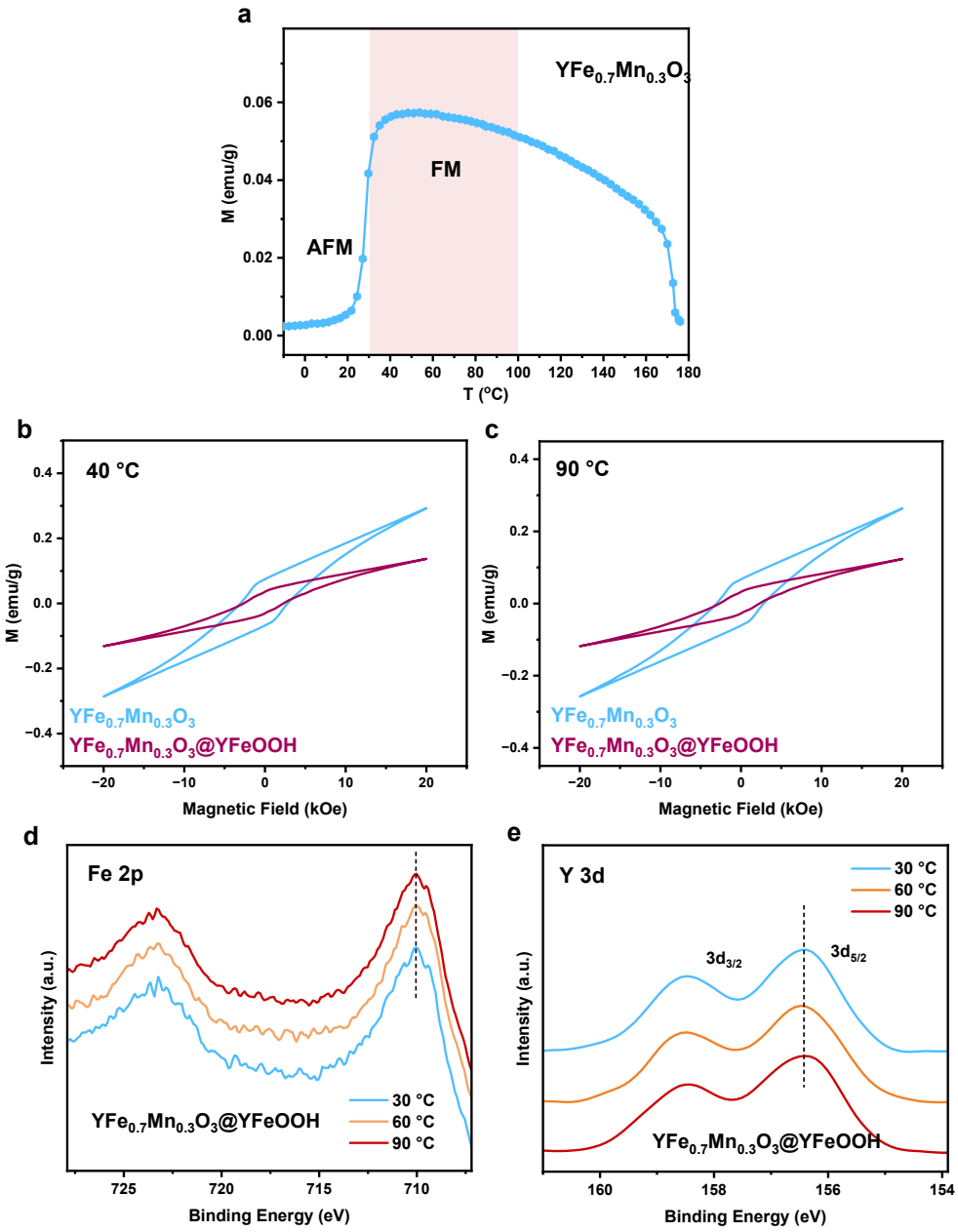

Fig. S20 The thermal magnetic properties of $YFe_{0.7}Mn_{0.3}O_3$ and $YFe_{0.7}Mn_{0.3}O_3$@YFeOOH and elemental valence states of $YFe_{0.7}Mn_{0.3}O_3$@YFeOOH under thermal stimulation. (a) Field cooled magnetization curves for $YFe_{0.7}Mn_{0.3}O_3$ at an applied field of 100 Oe. (b, c) Magnetic hysteresis loops for $YFe_{0.7}Mn_{0.3}O_3$ and $YFe_{0.7}Mn_{0.3}O_3$@YFeOOH at 60 °C. (d, 4) Fe 2p and Y 3d XPS spectra for $YFe_{0.7}Mn_{0.3}O_3$@YFeOOH at different temperatures.

In 30-100 °C, the $YFe_{0.7}Mn_{0.3}O_3$ maintain canted antiferromagnetic state.

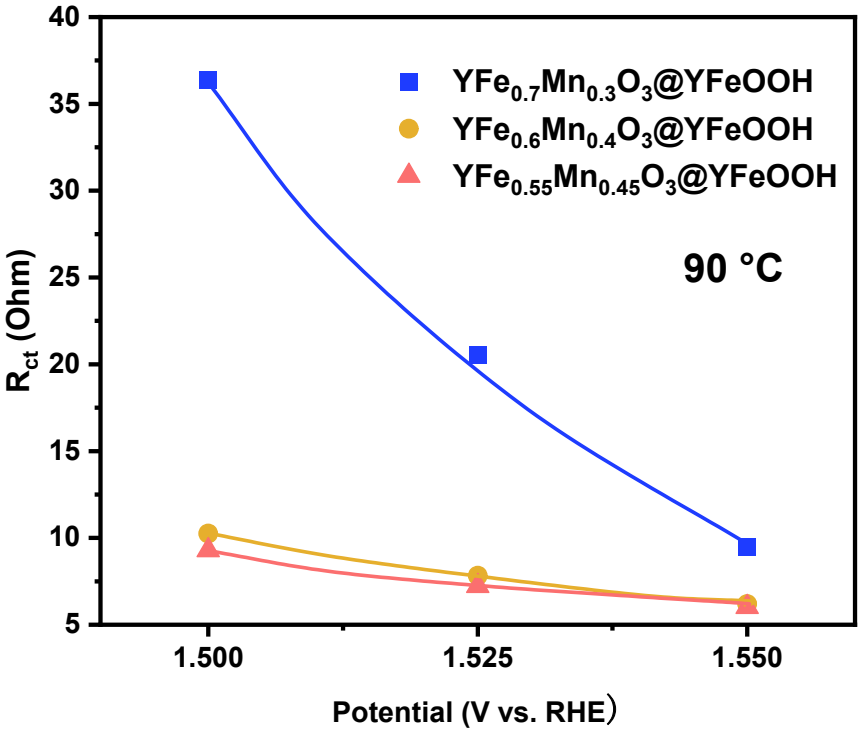

Fig. S21 Temperature-dependent R_{ct} fitted from EIS data in the OER potential regions of $YFe_{0.7}Mn_{0.3}O_3$@YFeOOH , $YFe_{0.6}Mn_{0.4}O_3$@YFeOOH and $YFe_{0.55}Mn_{0.45}O_3$@YFeOOH at 90 °C.

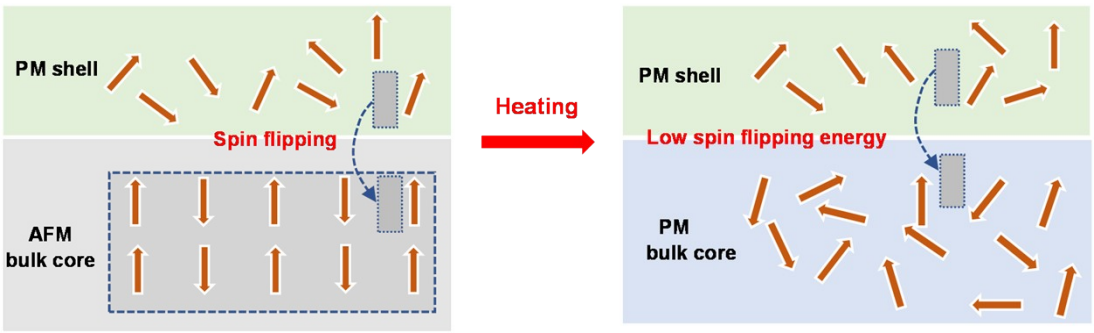

Fig. S22 The temperature-dependent spin-related electron transfer at the interface between $YFe_{0.55}Mn_{0.45}O_3$ core and YFeOOH shell.

Table S1. The element content of Fe and Mn determined by inductively coupled plasma optical emission spectrometer (ICP-OES).

Samples	Element content (mg/kg)		Molar content (%)	
	Fe	Mn	Fe	Mn
$YFe_{0.7}Mn_{0.3}O_3$	56375.21	24913.26	68.8	31.2
$YFe_{0.6}Mn_{0.4}O_3$	59703.70	39611.11	59.5	40.5
$YFe_{0.55}Mn_{0.45}O_3$	55874.24	47243.25	55.2	44.8

Table S2. The molar amount for Y and Fe in the surface layer of $YFe_{1-x}Mn_xO_3$ (x = 0.3, 0.4, and 0.45) after activation. The data were obtained by XPS analysis.

Samples	Element content (At. %)	
	Y 3d	Fe 2p

$YFe_{0.7}Mn_{0.3}O_3$@YFeOOH	19.2	19
$YFe_{0.6}Mn_{0.4}O_3$@YFeOOH	19	18.6
$YFe_{0.55}Mn_{0.45}O_3$@YFeOOH	19.3	18.7

Table S3. Elemental ratio of Y and Fe at different etching depths of $YFe_{0.6}Mn_{0.4}O_3$@YFeOOH.

Etching depth (nm)	Y/Fe ratio
0	1 : 1
2	1.08 : 1
4	1. 12 : 1
6	1.19 : 1
10	1.63 : 1
20	1.71 : 1

Table S4. The effects of temperature on reference electrode potential and pH in 1.0 M KOH.

Temperature (°C)	$\Delta E_{Hg/HgO}$ (V)	[a] E_{RHE} (V)	[b] E^{o}_{H2O} (V)
30	0.9158	$E_{Hg/HgO}$ + 0.9158	1.2245
35	0.9142	$E_{Hg/HgO}$ + 0.9142	1.2200
40	0.9126	$E_{Hg/HgO}$ + 0.9126	1.2155
45	0.9106	$E_{Hg/HgO}$ + 0.9106	1.2110
50	0.9078	$E_{Hg/HgO}$ + 0.9078	1.2065
55	0.9060	$E_{Hg/HgO}$ + 0.9060	1.2020
60	0.9040	$E_{Hg/HgO}$ + 0.9040	1.1975
65	0.9015	$E_{Hg/HgO}$ + 0.9015	1.1930
70	0.8988	$E_{Hg/HgO}$ + 0.8988	1.1885
75	0.8957	$E_{Hg/HgO}$ + 0.8957	1.1840
80	0.8929	$E_{Hg/HgO}$ + 0.8929	1.1795
85	0.8890	$E_{Hg/HgO}$ + 0.8890	1.1750
90	0.8850	$E_{Hg/HgO}$ + 0.8850	1.1705
95	0.8810	$E_{Hg/HgO}$ + 0.8810	1.1660
100	0.8770	$E_{Hg/HgO}$ + 0.8770	1.1620

[a] According to the Nernst equation of $E_{RHE} = E_{ref} + (2.303RT/nF)pH + E^{e}_{ref}$, we could know that the reversible hydrogen potential (RHE) is related with temperature. Thus, the effect of temperature on the Hg/HgO reference electrode potential was corrected by a potential corrective term of $\Delta E_{Hg/HgO}$, which was tested by the open circuit voltage in two electrode system comprising of a Hg/HgO electrode and a standard hydrogen electrode.

[b] The temperature-dependent theoretical thermodynamic water splitting potential (E^{o}_{H2O}) is calculated by an empirical equation of $E^{o}_{H2O} = 1.229 - 0.9 \times 10^{-3} (T - 298)$[4].

Table S5. Fitting parameters of EIS data for $YFe_{0.6}Mn_{0.4}O_3$@YFeOOH using the equivalent circuit proposed in the inset in Fig. 4d.

Temperature (°C)	Potential (V vs RHE)	R_s (Ω)	CPE-T	CPE-p	R_{ct} (Ω)	C_{ct} (μF)
30	1.450	5.5394	0.0004482	0.84588	6017	2.8540
	1.475	5.536	0.0006605	0.83524	3892	3.9191
	1.500	5.53	0.0009886	0.92214	1499	33.784
	1.525	5.504	0.00101	0.92075	1050	33.869
	1.550	5.486	0.00102	0.92283	495.6	35.302
60	1.450	4.519	0.0008023	0.88995	502.6	14.856
	1.475	4.508	0.00141	0.90427	322.4	38.341
	1.500	4.499	0.0016	0.89923	193.8	41.244
	1.525	4.47	0.00172	0.90184	139	46.749
	1.550	4.396	0.00173	0.91011	87.34	53.287
90	1.450	3.559	0.00229	0.86069	17.11	53.118
	1.475	3.557	0.00366	0.86598	13.25	66.223
	1.500	3.549	0.00403	0.86919	10.25	78.275
	1.525	3.445	0.00438	0.87239	7.823	90.451
	1.550	3.323	0.00442	0.88808	6.186	121

Table S6. Fitting parameters of EIS data for $YFe_{0.55}Mn_{0.45}O_3$@YFeOOH using the equivalent circuit proposed in the inset in Supplementary Fig. 6e.

Temperature (°C)	Potential (V vs RHE)	R_s (Ω)	CPE-T	CPE-p	R_{ct} (Ω)	C_{ct} (μF)
	1.450	4.699	0.0001685	0.86103	5050	1.0440
	1.475	4.693	0.001755	0.87085	2790	1.4029
30	1.500	4.195	0.00101	0.92456	985	35.202
	1.525	4.146	0.00103	0.92487	741.3	36.23
	1.550	4.141	0.00105	0.93212	415.9	41.139
	1.450	3.41	0.00364	0.87224	14.86	72.308
	1.475	3.302	0.00433	0.88303	11.88	105
90	1.500	3.265	0.0046	0.88614	9.286	118
	1.525	3.2	0.00517	0.87694	7.233	119
	1.550	3.179	0.005	0.8789	6.021	116

Table S7. Fitting parameters of EIS data for $YFe_{0.7}Mn_{0.3}O_3$@YFeOOH using the equivalent circuit proposed in the inset in Supplementary Fig. 9e.

Temperature (°C)	Potential (V vs RHE)	R_s (Ω)	CPE-T	CPE-p	R_{ct} (Ω)	C_{ct} (μF)
30	1.450	5.573	0.0009125	0.90125	939.6	11.1
	1.475	5.57	0.00122	0.91093	651.3	36.401
	1.500	5.542	0.00144	0.90456	477.1	40.171
	1.525	5.384	0.00153	0.90027	293.1	40.353
	1.550	5.309	0.00192	0.88226	173.9	40.347
60	1.450	5.208	0.0006803	0.92782	453.1	23.774
	1.475	5.192	0.00113	0.93991	278.7	51.119
	1.500	5.179	0.00141	0.92127	165.4	50.303
	1.525	5.177	0.00202	0.90527	115.5	60.941
	1.550	5.174	0.00221	0.89578	76.8	58.844
90	1.450	4.708	0.00388	0.85159	88.66	61.539
	1.475	4.68	0.00473	0.85023	59.56	78.753
	1.500	4.644	0.00564	0.85724	36.37	110
	1.525	4.585	0.0058	0.86277	20.51	122
	1.550	4.049	0.00585	0.87061	9.5	132

Supplementary references

1. P. Mandal, C. Serrao, E. Suard, V. Caignaert, B. Raveau, A. Sundaresan and C. Rao, *J.*

Solid State Chem. 2013, ***197,*** 408-413.
2. S. Geller and E. Wood, *Acta Crystallogr.* 1956, **9,** 563-568.
3. N. Cohen and O. Diéguez, *Phys. Rev. B* 2021, **104,** 064111.
4. A. Awasthi, K. Scott and S. Basu, Int. *J. Hydrogen Energ.* 2011, **36**, 14779-14786.